

Cathodic shift of onset potential on TiO_2 nanorod arrays with significantly enhanced visible light photoactivity via nitrogen/cobalt co-implantation

Xianyin Song(宋先印), Hongtao Zhou(周洪涛), Changzhong Jiang(蒋昌忠)
Citation: Chin. Phys. B, 2021, 30 (**5**): 058505. DOI: 10.1088/1674-1056/abee07
Journal homepage: http://cpb.iphy.ac.cn; http://iopscience.iop.org/cpb

What follows is a list of articles you may be interested in

Experimental and computational study of visible light-induced photocatalytic ability of nitrogen ions-implanted TiO_2 nanotubes

Ruijing Zhang(张瑞菁), Xiaoli Liu(刘晓丽), Xinggang Hou(侯兴刚), Bin Liao(廖斌)
Chin. Phys. B, 2020, 29 (**4**): 048501. DOI: 10.1088/1674-1056/ab6d53

Research on the radiation hardened SOI devices with single-step Si ion implantation

Li-Hua Dai(戴丽华), Da-Wei Bi(毕大炜), Zhi-Yuan Hu(胡志远), Xiao-Nian Liu(刘小年), Meng-Ying Zhang(张梦映), Zheng-Xuan Zhang(张正选), Shi-Chang Zou(邹世昌)
Chin. Phys. B, 2018, 27 (**4**): 048503. DOI: 10.1088/1674-1056/27/4/048503

Improved performance of Ge n^+/p diode by combining laser annealing and epitaxial Si passivation

Chen Wang(王尘), Yihong Xu(许怡红), Cheng Li(李成), Haijun Lin(林海军)
Chin. Phys. B, 2018, 27 (**1**): 018502. DOI: 10.1088/1674-1056/27/1/018502

Low frequency noise and radiation response in the partially depleted SOI MOSFETs with ion implanted buried oxide

Liu Yuan, Chen Hai-Bo, Liu Yu-Rong, Wang Xin, En Yun-Fei, Li Bin, Lu Yu-Dong
Chin. Phys. B, 2015, 24 (**8**): 088503. DOI: 10.1088/1674-1056/24/8/088503

Preparation of graphene on Cu foils by ion implantation with negative carbon clusters

Li Hui, Shang Yan-Xia, Zhang Zao-Di, Wang Ze-Song, Zhang Rui, Fu De-Jun
Chin. Phys. B, 2015, 24 (**1**): 018502. DOI: 10.1088/1674-1056/24/1/018502

SPECIAL TOPIC — Ion beam modification of materials and applications

Cathodic shift of onset potential on TiO_2 nanorod arrays with significantly enhanced visible light photoactivity via nitrogen/cobalt co-implantation*

Xianyin Song(宋先印), Hongtao Zhou(周洪涛), and Changzhong Jiang(蒋昌忠)†

College of Materials Science and Engineering, Hunan University, Changsha 410082, *China*

(Received 7 January 2021; revised manuscript received 24 February 2021; accepted manuscript online 12 March 2021)

Despite anionic doping has been widely implemented to increase the visible light activity of TiO_2, it often gives rise to a dramatical anodic shift in current onset potential. Herein, we show an effective method to achieve the huge cathodic shift of TiO_2 photoanode with significantly enhanced visible light photo-electrochemical activity by nitrogen/cobalt co-implantation. The nitrogen/cobalt co-doped TiO_2 nanorod arrays (N/Co-TiO_2) exhibit a cathodic shift of 350 mV in onset potential relative to only nitrogen-doped TiO_2 (N-TiO_2). Moreover, the visible-light ($\lambda > 420$ nm) photocurrent density of N/Co-TiO_2 reaches 0.46 mA/cm^2, far exceeding 0.07 mA/cm^2 in N-TiO_2 at 1.23 V *versus* reversible hydrogen electrode (RHE). Systematic characterization studies demonstrate that the enhanced photo-electrochemical performance can be attributed to the surface synergic sputtering of high-energy nitrogen/cobalt ions.

Keywords: ion implantation, TiO_2, surface sputtering, photo-electrochemical water splitting

PACS: 85.40.Ry, 71.20.Nr, 68.49.Sf, 89.60.–k **DOI:** 10.1088/1674-1056/abee07

1. Introduction

Since Fujishima and Honda reported the photo-oxidation of water on TiO_2 in 1972,[1] TiO_2 has been extensively investigated as a photoanode material due to its high water-oxidation activity, excellent photostability, and earth abundance.[2–4] However, the poor visible light photo-activity induced by its wide band gap ($E_g = 3.0$ eV) is the major limitation for its further application as photo-anode.[5] Although anionic doping (*e.g.*, N, S) could effectively increase the visible-light response of TiO_2, it also causes a significant anodic shift in current onset potential.[6–8] And this can be ascribed to the introduced impurity states above the valence band maximum (VBM) and large number of surface lattice defects, which decrease the oxidative capability and surface transfer dynamics of photo-generated holes.[9,10] Meanwhile, the onset potential of photo-anodes plays a critical role in building highly efficient and unassisted hetero-type PEC water-splitting cells.[11–13]

To reduce the onset potential, the most commonly used method is loading various oxygen evolution catalysts on anion-doped TiO_2.[8,14] This method could efficiently decrease onset potential; however, the loaded electrocatalyst layers were easy to fall off and even affected the light-harvesting of the underneath semiconductor. Besides, Jang *et al.* reported another re-growth strategy to reduce structural disorders at the surface of photoanodes and had achieved cathodic shift in turn-on voltage.[11] However, this method is uncontrollable. Therefore, a general approach with high controllability is still desired.

Ion implantation, a typical surface engineering technology, has been widely used to tailor the electronic properties of semiconductor in industry.[15] It is a general method for introducing different and/or multiple elements of interest into semiconductor for systematic studies.[7] The implanted ions are presented in a highly dispersed state in the TiO_2 lattice.[10,16] Meanwhile, as a compulsive doping approach, high-energy ion bombardment could not only produce lattice defects, but also induce surface sputtering effect.[17–19]

Herein, considering the high controllability at impurity distribution and surface sputtering effect of ion implantation technology,[16,20] we used ion-implantation approach to co-dope nitrogen and cobalt into TiO_2 nanorods for PEC water oxidation (Fig. 1(a)). Our results demonstrate that the surface lattice disorder of N-TiO_2 can be effectively removed by surface synergic sputtering of nitrogen/cobalt ions. And the surface synergic sputtering endows a cathodic shift of 350 mV in onset potential and more than 6.5 times increase of visible light photo-activity for N/Co-TiO_2 samples, relative to only nitrogen doping (N-TiO_2). Our results demonstrated ion implantation was a novel and useful strategy for cathodic shift of TiO_2 photo-anode with improved catalytic activity.

*Project supported by the National Natural Science Foundation of China (Grant No. 11875211), the Major Science and Technology Program of Changsha, China (Grant No. kq1902046), and the Fundamental Research Funds for the Central Universities, China.

†Corresponding author. E-mail: czjiang@hnu.edu.cn

© 2021 Chinese Physical Society and IOP Publishing Ltd

2. Methods

2.1. Sample preparation

The TiO_2 nanorod array was grown on FTO glass via a well-developed hydrothermal method.[21] The obtained TiO_2 nanorod arrays were then annealed at temperature 550 °C for 3 hours in air. The nitrogen ions and cobalt ions were co-implanted into the TiO_2 nanorod array using a Kaufman ion source and a metal vapor vacuum arc (MEVVA) ion source implanter, respectively. The as-implanted TiO_2 were finally annealed at 550 °C for 3 hours in high vacuum (approximately 10^{-4} Pa) (Fig. 1(b)). The nitrogen-doped and cobalt-doped TiO_2 nanorod arrays were also prepared via ion implantation and subsequent high-vacuum annealing procedures.

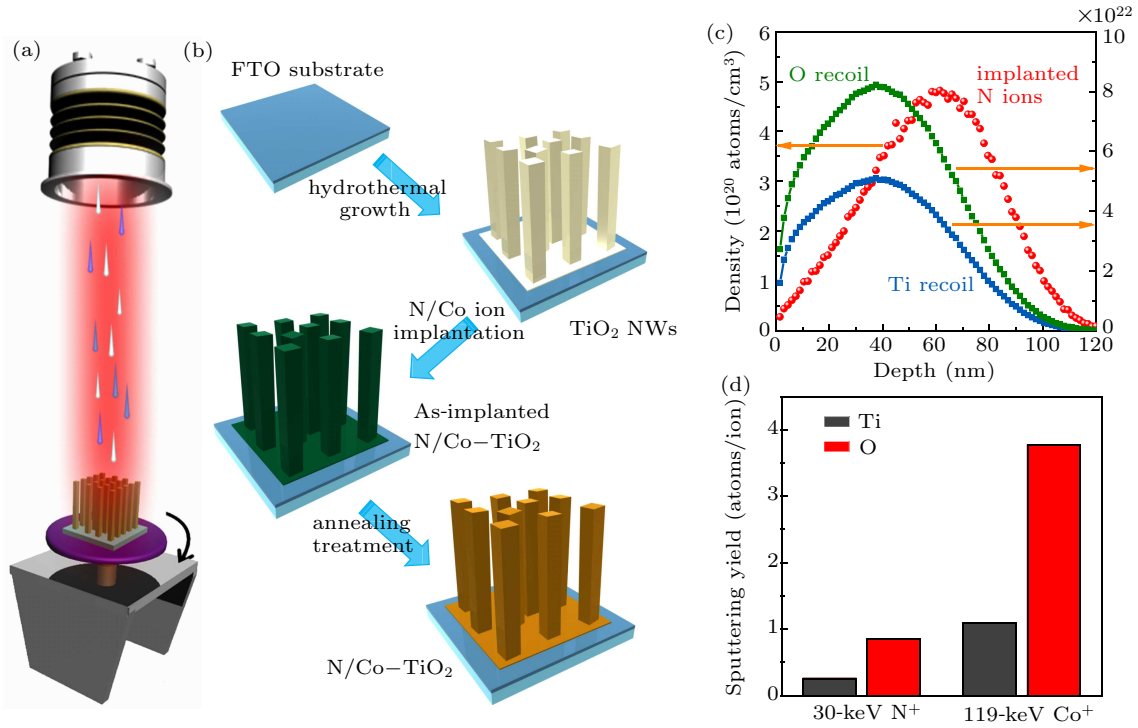


Fig. 1. (a) Simplified diagram schematic of N/Co ion co-implantation. (b) Schematic diagram of the fabrication process of N/Co-TiO_2 by ion implantation method. (c) SRIM calculated concentration profiles of N ions and damage (Ti recoil and O recoil) in TiO_2 at the implantation energy of 30 keV to a dose of 3×10^{15} ions/cm^2. (d) SRIM simulated surface sputtering yield by 30-keV N ions and 119-keV Co ions.

2.2. Photo-electrochemical measurements

Photo-electrochemical (PEC) measurements were performed in a three-electrode cell under a solar simulator (a 500-W xenon lamp coupled with an AM 1.5 G filter) at an illumination intensity of 100 mW/cm^2. The TiO_2 photo-anodes were used as working electrodes, and a Pt foil was used as a counter electrode. An Ag/AgCl (saturated KCl) electrode was served as reference electrodes and 1.0-M NaOH aqueous solution (pH = 13.6) was used as the electrolyte. The illuminated area was fixed at 0.785 cm^2 (a sealing ring with 1 cm in diameter). The measured potentials were converted to reversible hydrogen electrode (RHE) potential according to the Nernst equation

$$\begin{aligned} E_{\mathrm{RHE}}(\mathrm{V}) &= E_{\mathrm{Ag/AgCl}} + E^{\mathrm{o}}_{\mathrm{Ag/AgCl}} + 0.059 \times \mathrm{pH} \\ &= E_{\mathrm{Ag/AgCl}} + 1\ \mathrm{V}. \end{aligned}$$

2.3. Material characterization

Scanning electron microscopy (SEM) was performed on a JEOL S-4800 microscope. Transmission electron microscopy (TEM) were carried out on a JEOL JEM2010. X-ray diffraction (XRD) patterns were recorded using a Bruker AXS, D8 Advance x-ray powder diffractometer with Cu-Kα irradiation (wavelength 1.5418 Å). Raman spectroscopy was collected using a commercial Raman microscope (HR800, Horiba) and a laser emitting at 488 nm was served as the excitation source. X-ray photoelectron spectroscopy (XPS) experiments were done on a Thermo Scientific ESCALAB 250Xi system using Al Kα radiation source of 1486.6 eV, with C 1s (284.8 eV) as calibration reference.

3. Results and discussion

3.1. SRIM simulation

An implanted high-energy ion will lose its energy through a series of cascade collisions with the target atomic nucleus and extranuclear electrons, and its distribution law in the target material is clearly recognized and well determined. We can accurately design the depth distribution of dopant ions in TiO_2 through adjusting the ion implantation energy.

Besides, the atomic collision can transfer enough energy to target atoms to produce irradiation damage and surface sputtering. Figure 1(c) shows the calculated concentration profiles for implanted N ions, as well as damages (Ti recoil and O recoil) in TiO_2 according to SRIM simulation. The simulations show the maximum defect damage is much closer to the surface than the maximum N ion location. Meanwhile, the simulated surface sputtering yield of TiO_2 is shown in Fig. 1(d). Clearly, the sputtering yield induced by 119-keV Co ion is much higher than that of 30-keV N ion. In addition, the sputtering yield of lattice oxygens is more than twice than that of Ti atoms, showing preferential sputtering to oxygen atoms. This is consistent with previous experiment reports.[18,20]

3.2. Structure characterization

Figures 2(a)–2(h) show the SEM images of the original TiO_2, N-TiO_2, Co-TiO_2, and N/Co-TiO_2. The pristine TiO_2 nanorod presents a smooth side face and rectangular cross section with some bumps at the top. And the morphology of N-TiO_2 and Co-TiO_2 do not exhibit obvious changes compared to the pristine TiO_2. However, the rough cross-section at the top of nanorods becomes smoother for N/Co-TiO_2 samples (Figs. 2(g)–2(h)). Meanwhile, the N, Co co-implanted TiO_2 samples without subsequent annealing treatment (as-implanted N/Co-TiO_2) have already presented smoother cross-section at the top, as shown in Fig. S1 in Supporting information. It means TiO_2 nanorod tip can be effectively etched by the synergic sputtering of high-energy nitrogen ions and cobalt ions. It is worth noting that the irradiation damages at the top of TiO_2 nanorod have been effectively removed at the same time, confirmed by the HRTEM results as shown in Fig. S2. Besides, figures S3(a)–S3(b) also show that the surface etching become more evident as increasing the cobalt ion dose. The surface sputtering yield and ion irradiation induced surface patterns are affected by multiple factors, such as ion species, ion energy, crystal orientation, temperature of substrate materials, *etc*.[17,19,21] While, it needs to be emphasized that the surface synergic sputtering of N/Co ions is not the simple dose superimposed effect, as these surface etching is obviously different from our previous C/N ion co-implantation and high-dose Cr ion implantation.[10,16] Even though, the inherent mechanism of synergic sputtering by N/Co ions here needs to be further studied.

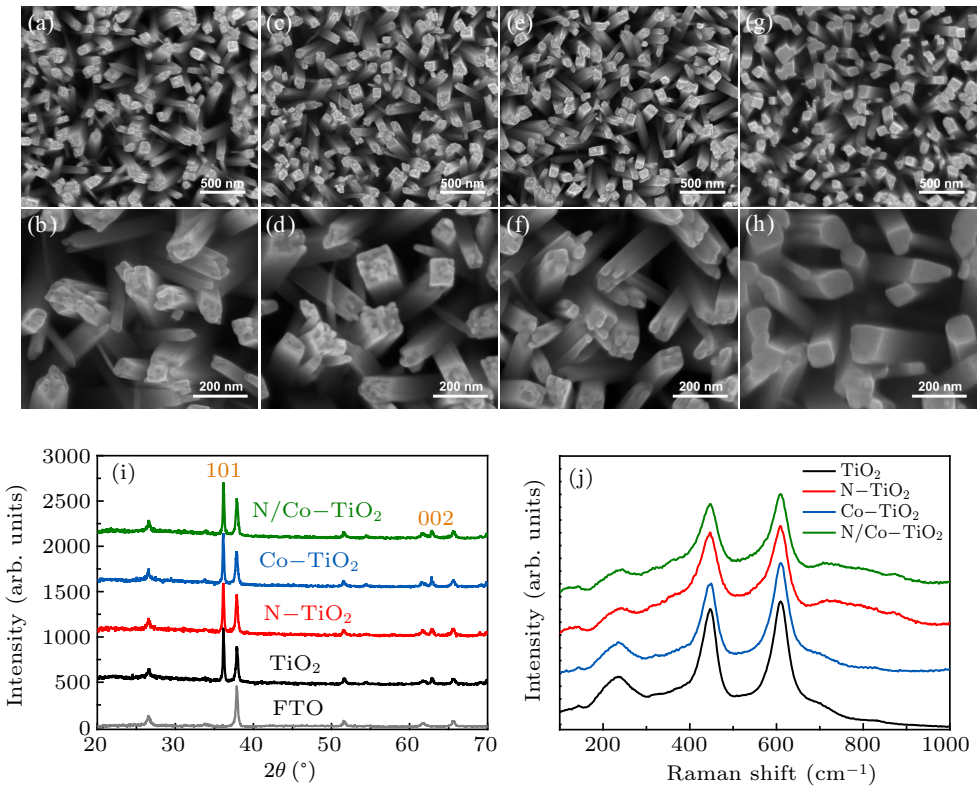


Fig. 2. SEM images of [(a) and (b)] the pristine TiO_2, [(c) and (d)] nitrogen-doped TiO_2 with a nitrogen dose of 3×10^{15} ions/cm^2 (N-TiO_2), [(e) and (f)] cobalt-doped TiO_2 with a cobalt dose of 3×10^{15} ions/cm^2 (Co-TiO_2), [(g) and (h)] nitrogen/cobalt co-doped TiO_2 with a nitrogen dose of 3×10^{15} ions/cm^2 and a cobalt dose of 3×10^{15} ions/cm^2 (N/Co-TiO_2). (i) XRD patterns of FTO, pristine TiO_2, N-TiO_2, Co-TiO_2, and N/Co-TiO_2. (j) Raman spectra of pristine TiO_2, N-TiO_2, Co-TiO_2, and N/Co-TiO_2.

Figure 2(i) displays the XRD patterns of FTO substrate, pristine TiO_2, N-TiO_2, Co-TiO_2, and N/Co-TiO_2. It is indicated that all the samples were rutile phase TiO_2[22] and no additional phase was detected after ion implantation and annealing, even for high-dose ion implantation samples (Fig. S3(c)). It further demonstrates that the implanted ions are

presented in a highly dispersed state in the TiO_2 lattice via ion-implantation method. Raman spectroscopy studies also confirmed the conclusion of XRD analysis. There are four typical Raman-active modes with frequencies at 610, 447, 235, and 141 cm^{-1} (Fig. 2(j) and Fig. S3 (d)), corresponding to the A1g, Eg, multi-photon and B1g modes of the rutile space group ($P42/mnm$), respectively.[23] However, it is also noteworthy that some new modes emerge at the range from 700 cm^{-1} to 900 cm^{-1} for nitrogen-doped TiO_2, suggesting structural changes occurred after doping.[2]

3.3. Photo-electrochemical measurement

PEC performances were investigated under a simulated solar irradiation of 100 mW/cm^2 with or without through a visible-light cutoff filter of 420 nm. Figure 3(a) shows the linear sweep voltammogram collected for pristine TiO_2, N-TiO_2, and N/Co-TiO_2 under dark and AM 1.5 G irradiation. Compared to the pristine TiO_2, the N-TiO_2 sample exhibits an enhanced photocurrent density under high-bias voltages ($>$ 1.6 V *versus* RHE), but nearly 0.6-V anodic shift in current onset potential is observed, which directly leads to a much lower photocurrent density (0.17 mA/cm^2) at the typical voltage of 1.23 V *versus* RHE. However, as the Co ions was subsequently implanted into N doped TiO_2, the photocurrent density of N/Co-TiO_2 sample reaches 0.73 mA/cm^2 at 1.23 V *versus* RHE under simulated solar irradiation, which is more than twice higher than that of the pristine TiO_2 (0.33 mA/cm^2) obtained at the same potential. Most importantly, relative to the negligible visible-light response of pristine TiO_2 as expected, the N/Co-TiO_2 sample showed a significant cathodic shift of 350 mV in onset potential and more than 6.5 times increase of visible-light catalytic activity than that of N-TiO_2 (0.46 mA/cm^2 *versus* 0.07 mA/cm^2 at 1.23 V *versus* RHE) (Fig. 3(b)). In addition, the visible-light PEC activity of Co-TiO_2 was also studied. Figure S4 in Supporting information shows the increase of visible-light catalytic activity for Co-TiO_2 is slight and negligible.

The dosage effects of N/Co ions on PEC performance were also studied (Fig. 3(c)). The optimized PEC performance for N/Co co-implanted TiO_2 was obtained with an implantation ion fluence of 3×10^{15} ions/cm^2 nitrogen and 3×10^{15} ions/cm^2 cobalt. Further increase of cobalt implantation dose can induce a decrease in photo-activity. The excessive Co ion implantation could produce other irreparable surface lattice damages that also can act as the recombination centers to degrade the overall photo-activity, despite high-dose Co doped TiO_2 (Co^+-TiO_2) shows enhanced visible-light catalytic activity (see Fig. S5).

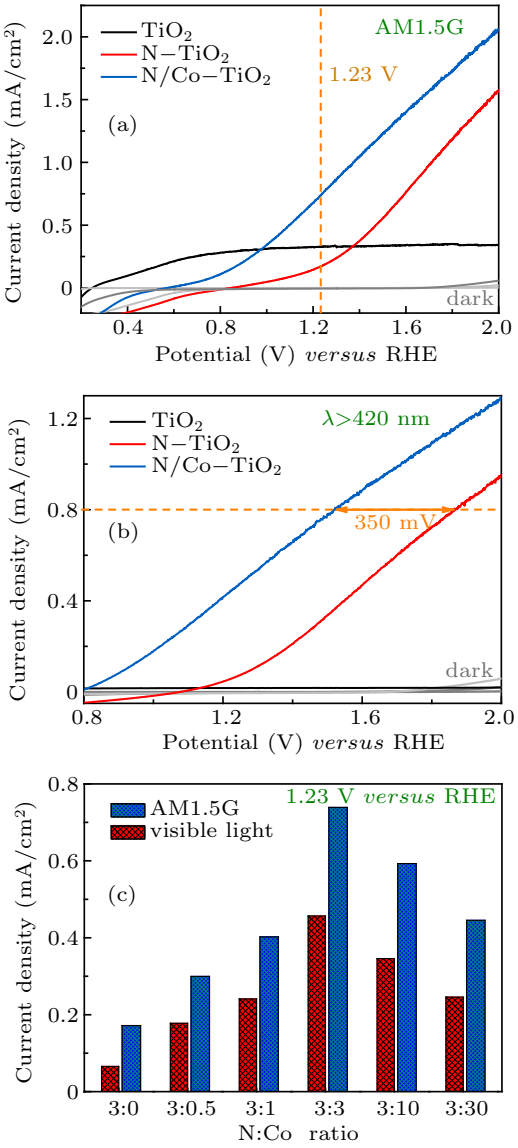


Fig. 3. (a) Linear sweep voltammetry of TiO_2, N-TiO_2, and N/Co-TiO_2 under AM 1.5 G irradiation. (b) Linear sweep voltammetry of TiO_2, N-TiO_2, and N/Co-TiO_2 under visible light irradiation. (c) The histograms of AM 1.5 G and visible-light photocurrent density for N/Co co-doped TiO_2 with different cobalt doses to the same nitrogen dose of 3×10^{15} ions/cm^2.

3.4. Chemical state analysis

XPS measurements were carried out to further investigate the chemical states of N and Co atoms in TiO_2, particularly for N-TiO_2 and N/Co-TiO_2 samples. The survey spectrum of N/Co-TiO_2 sample shows the presence of weak N and Co signals (Fig. S6(a)), and the carbon signals were used for calibration of the binding energy (Fig. S6(b)). Figure 4(a) shows N 1s spectra of N-TiO_2 and N/Co-TiO_2 samples. There are several broad peaks from 394 eV to 404 eV, which can be deconvolved into three peaks located at around 402, 400, and 396 eV corresponding to the chemical bonding of N–N, N–O, and N-Ti bonds, respectively.[7,8] Between them, the substitution N-Ti states are mainly responsible for the visible light absorption according to previous theoretical and experimental evidences.[8,24,25] A negative shift ($\sim$ 0.26 eV) of N-Ti peak can be observed in N/Co-TiO_2 samples, suggesting the in-

creasing electron density around N atoms. However, this shift cannot be ascribed to the N–Co interaction, because the binding energy of N–Co is stronger than N-Ti bonding.[8,26]

Figure 4(b) shows the XPS Co 2p spectra of Co-TiO_2 and N/Co-TiO_2. Two peaks centered at 781 eV and 796.5 eV are observed, which can be assigned to Co $2p_{3/2}$ and Co $2p_{1/2}$ of Co^{2+} in TiO_2, respectively.[27,28] And it can be seen that two satellite peaks located at approximately 786.6 eV and 802.8 eV appeared, which also can be ascribed to Co^{2+} species,[27] consistent with the literature values of Co-doped TiO_2.[29,30] Impressively, the Co 2p spectrum of N/Co-TiO_2 also exhibits a negative shift in binding energy. Meanwhile, similar shift to lower energy region for N/Co-TiO_2 samples is also observed in XPS Ti 2p and O 1s spectra, compared to N-TiO_2 as shown in Figs. 4(c)–4(d). The negative shift in XPS spectra of N/Co-TiO_2 can be ascribed to the excess electrons from oxygen vacancies transferring to other atoms. And the more oxygen vacancies incorporated into N/Co-TiO_2 can arise from the preferential sputtering of lattice oxygen in TiO_2 by high-energy N/Co ions, which has confirmed in Figs. 1(d) and 2(g)–2(h).

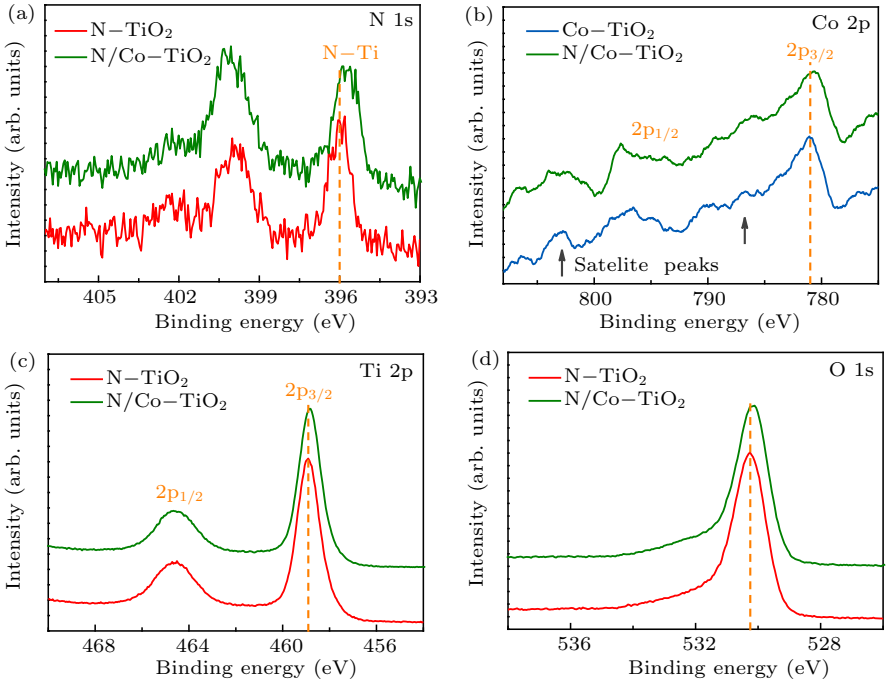


Fig. 4. (a) XPS N 1s spectra of N-TiO_2 and N/Co-TiO_2, (b) XPS Co 2p spectra of Co-TiO_2 and N/Co-TiO_2, (c) XPS Ti 2p spectra, and (d) O 1s spectra of N-TiO_2 and N/Co-TiO_2.

3.5. Electrochemical characterization

To further clarify the intrinsic electronic properties of N-TiO_2 and N/Co-TiO_2, we have performed electrochemical impedance investigations. The Mott–Schottky plots was used to calculate the carrier densities and flat band potential at the electrode/electrolyte interface according to the equations given below:

$$N_{\mathrm{d}} = (2/\varepsilon\varepsilon_0 e_0)\left[\frac{\mathrm{d}\left(1/C^2\right)}{\mathrm{d}V}\right]^{-1}, \tag{1}$$

$$1/C^2 = (2/\varepsilon\varepsilon_0 e_0 N_{\mathrm{d}})\left[(V - V_{\mathrm{FB}}) - KT/e_0\right], \tag{2}$$

where ε is the dielectric constant of rutile TiO_2 ($\varepsilon = 170$),[5] ε_0 is the permittivity of vacuum, e_0 is the electron charge, V is the applied potential, C is the capacitance between TiO_2 and electrolyte (in units of $\mathrm{F{\cdot}cm^{-2}}$), N_{d} is the carrier density, V_{FB} is the flat band potential, K is the Boltzmann constant, and T is the absolute temperature (in unit K). In Fig. 5(a) and Fig. S7, the positive slope of Mott–Schottky plots indicates the n-type semiconductor characteristics. Obviously, the N/Co-TiO_2 exhibits a smaller slope than TiO_2 and N-TiO_2, indicating a much higher donor density. The carrier densities of TiO_2, N-TiO_2, and N/Co-TiO_2 calculated from Eq. (1) are 1.88×10^{17}, 1.21×10^{21}, and 2.43×10^{21} $\mathrm{cm^{-3}}$, respectively. The increased donor concentration of N/Co-TiO_2 is mainly attributed to the incorporated oxygen vacancies by high-vacuum annealing and preferential sputtering of lattice oxygen. And these oxygen vacancies could serve as electron donors in TiO_2[5,7] and enhance the charge separation efficiency from bulk to surface.[7,8]

However, large numbers of surface and bulk defects are also introduced during the ion implantation. Although partial of lattice defects have been repaired after subsequent heat treatments, many defects still survived at the surface of N-doped TiO_2 (Fig. S2(b)), especially under high-dose ion implantation. These surface lattice disorders act as deep energy level, which can result in Fermi level pinning and a significant anodic shift of the flat band potential (V_{FB}).[11,20,31] Fortunately, these surface defects have been effectively removed through the surface synergic sputtering induced by

high-energy N/Co ions (Fig. S2). Therefore, the N/Co-TiO_2 sample displays a huge cathodic shift of V_{FB} and onset potential, relative to the N-TiO_2 (Figs. 5(a) and 3(a)).

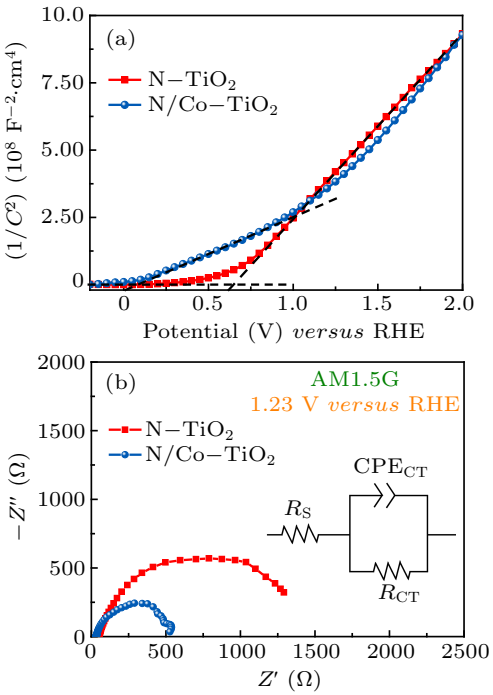


Fig. 5. (a) Mott–Schottky curves for N-TiO_2 and N/Co-TiO_2 samples collected at the frequency of 1 kHz in dark. (b) Nyquist plots obtained at a potential of 1.23 V (*versus* RHE) under AM 1.5G irradiation.

Finally, we will further investigate the charge transfer properties at the TiO_2/electrolyte interfaces for N-TiO_2 and N/Co-TiO_2 through the electrochemical impedance spectroscopy (EIS). Figures 5(b) and S8 show the Nyquist plots of N-TiO_2 and N/Co-TiO_2 acquired from EIS measurements. All the Nyquist plots exhibited semi-circles and the data were well fitted by a typical Randles circuit model (insets, Fig. 5(b)), which consisted of the total series resistance (R_S), constant phase angle element (CPE_{CT}), and charge-transfer resistance (R_{CT}) at the TiO_2/electrolyte interfaces.[7,32] The fitted charge transfer resistance (R_{CT}) for N/Co-TiO_2 was less than half than that of N-TiO_2 (detailed values, see Table S1), indicating superior charge transfer kinetics of photo-generated carriers at the electrode/electrolyte interface for N/Co co-implanted TiO_2. As a consequence, the N/Co-TiO_2 samples show obviously increased PEC performances, compared to the N-TiO_2 (Fig. 3).

4. Conclusion

In summary, we have successfully achieved a huge cathodic shift in onset potential for TiO_2 photo-anode with significantly enhanced visible light photo-electrochemical performances through N/Co co-implantation. Due to the synergic sputtering of implanted N/Co ions, the surface lattice disorder induced by ion bombardment has been effectively removed. As a consequence, the N/Co co-implanted TiO_2 exhibits a cathodic shift of 350 mV in onset potential and more than 6.5 times increase of visible-light photocurrent density at 1.23 V *versus* RHE relative to only N-implanted TiO_2. Our work demonstrates that ion implantation technology is a powerful method to modulate the band structure of photo-electrodes, and thus improve their PEC performances. We believe ion implantation is a general strategy which can be extended to introduce different dopants into different semiconductor materials for PEC water splitting and possibly other applications such as solar cells and photodetectors.

References

[1] Fujishima A and Honda K 1972 *Nature* **238** 37
[2] Chen X, Liu L, Yu P Y and Mao S S 2011 *Science* **331** 746
[3] Sambur J B, Chen T Y, Choudhary E, Chen G, Nissen E J, Thomas E M, Zou N and Chen P 2016 *Nature* **530** 77
[4] Shaner M R, Hu S, Sun K and Lewis N S 2015 *Energy Environ. Sci.* **8** 203
[5] Wang G, Wang H, Ling Y, Tang Y, Yang X, Fitzmorris R C, Wang C, Zhang J Z and Li Y 2011 *Nano Lett.* **11** 3026
[6] Hoang S, Berglund S P, Hahn N T, Bard A J and Mullins C B 2012 *J. Am. Chem. Soc.* **134** 3659
[7] Song X, He D, Li W, Ke Z, Liu J, Tang C, Cheng L, Jiang C, Wang Z and Xiao X 2019 *Angew. Chem. Int. Edit.* **58** 16660
[8] Wang G, Xiao X, Li W, Lin Z, Zhao Z, Chen C, Wang C, Li Y, Huang X, Miao L, Jiang C, Huang Y and Duan X 2015 *Nano Lett.* **15** 4692
[9] Chen X and Burda C 2008 *J. Am. Chem. Soc.* **130** 5018
[10] Song X, Li W, Liu X, Wu Y, He D, Ke Z, Cheng L, Jiang C, Wang G, Xiao X and Li Y 2021 *J. Energy Chem.* **55** 154
[11] Jang J W, Du C, Ye Y, Lin Y, Yao X, Thorne J, Liu E, McMahon G, Zhu J, Javey A, Guo, J and Wang, D 2015 *Nat. Commun.* **6** 7447
[12] Liu C, Tang J, Chen H M, Liu B and Yang P 2013 *Nano Lett.* **13** 2989
[13] Wang Q, Hisatomi T, Jia Q, Tokudome H, Zhong M, Wang C, Pan Z, Takata T, Nakabayashi M, Shibata N, Li Y, Sharp I D, Kudo A, Yamada T and Domen K 2016 *Nat. Mater.* **15** 611
[14] Hoang S, Guo S, Hahn N T, Bard A J and Mullins C B 2012 *Nano Lett.* **12** 26
[15] Dearnaley G 1975 *Nature* **256** 701
[16] Song X, Li W, He D, Wu H, Ke Z, Jiang C, Wang G and Xiao X 2018 *Adv. Energy Mater.* **8** 1800165
[17] Song X, Dai Z, Xiao X, Li W, Zheng X, Shang X, Zhang X, Cai G, Wu W, Meng F and Jiang C 2015 *Sci. Rep.* **5** 17529
[18] Zheng X, Shen S, Ren F, Cai G, Xing Z, Liu Y, liu D, Zhang G, Xiao X, Wu W and Jiang C 2015 *Int. J. Hydrogen Energy* **40** 5034
[19] Ou X, Heinig K H, Hubner R, Grenzer J, Wang X, Helm M, Fassbender J and Facsko S 2015 *Nanoscale* **7** 18928
[20] Zhou X, Häublein V, Ning L, Nguyen N T, Zolnhofer E M, Tsuchiya H, Killian M S, Meyer K, Frey L and Schmuki P 2016 *Angew. Chem. Int. Edit.* **55** 3763
[21] Ou X, Keller A, Helm M, Fassbender J and Facsko S 2013 *Phys. Rev. Lett.* **111** 016101
[22] Liu B and Aydil E S 2009 *J. Am. Chem. Soc.* **131** 3985
[23] Narayanan P 1950 *Proceedings-Mathematical Sciences* **32** 279
[24] Asahi R, Morikawa T, Ohwaki T, Aoki K and Taga Y 2001 *Science* **293** 269
[25] Varley J B, Janotti A and Van de Walle C G 2011 *Adv. Mater.* **23** 2343
[26] Wang L, Zhang W, Zheng X, Chen Y, Wu W, Qiu J, Zhao X, Zhao X, Dai Y and Zeng J 2017 *Nat. Energy* **2** 869
[27] Liao L, Zhang Q, Su Z, Zhao Z, Wang Y, Li Y, Lu X, Wei D, Feng G and Yu Q 2014 *Nat. Nanotechnol.* **9** 69
[28] He D, Song X, Li W, Tang C, Liu J, Ke Z, Jiang C and Xiao X 2020 *Angew. Chem. Int. Ed.* **59** 6929
[29] Chambers S A, Wang C M, Thevuthasan S, Droubay T, McCready D E, Lea A S, Shutthanandan V and Windisch C F 2002 *Thin Solid Films* **418** 197
[30] Manivannan A, Seehra M S, Majumder S B and Katiyar R S 2003 *Appl. Phys. Lett.* **83** 111
[31] Dean M H and Stimming U 1989 *J. Phys. Chem.* **93** 8053
[32] Fang W, Wang X, Zhang H, Jia Y, Huo Z, Li Z, Zhao H, Yang H and Yao X 2014 *J. Mater. Chem. A* **2** 3513